www.czasopisma.pan.pl PAN POLSKA AKADEMIA NAUK www.journals.pan.pl

Arch. Metall. Mater. **67** (2022), 4, 1359-1370

DOI: https://doi.org/10.24425/amm.2022.141063

JUNFENG WANG[1], MIN XIA[1*], JIALUN WU[1], CHANGCHUN GE[2]

NOZZLE CLOGGING IN VACUUM INDUCTION MELTING GAS ATOMIZATION: INFLUENCE OF THE DELIVERY-TUBE AND NOZZLE COUPLING

Nozzle clogging seriously affects the continuity of spraying powder in vacuum induction melting gas atomization (VIGA) process and increases the consumption of gas and raw materials. However, there are few systematic studies on nozzle clogging. This paper reports the physics of nozzle clogging in gas atomization production. The influence of coupling-length of different melt delivery-tubes on nozzle clogging is studied numerically and experimentally. The interface tracking method of Volume of Fluid (VOF) and the large eddy simulation (LES) model are performed for visualizing the melt droplets flow traces in primary atomization and the associated simulation cloud images compared with experimental results. Four delivery-tube coupling-lengths (0 mm, 3 mm, 5 mm, and 7 mm) relative to nozzle position and two gas pressures (3 MPa and 4.5 MPa) are chosen for this study. The results indicated that the coupling-lengths of 0 mm and 3 mm increases the strength of the recirculation zone, the melt droplets backflow is obvious, and the nozzle is blocked. However, this phenomenon eliminated with increasing coupling-lengths, the atomization process is continuous, but the final fine powder yield decreases. This research is of guiding significance and reference for understanding the nozzle clogging of vacuum induction melting gas atomization (VIGA) technology.

Keywords: nozzle clogging; atomization; recirculation zone; delivery-tube

1. Introduction

Additive manufacturing (AM) exploits has empowered the powder metallurgy to energetically uphill across multiple industries namely automotive, marine and aerospace industries [1]. The manufacturing of metal powder with optimized geometries and near net shape size are not possible to achieved via conventional approaches [2]. Metal powder used in AM is required to have precise shape, optimized size and morphology. Gas atomization [3] remains a good choice owing to the quality, and purity of the obtained powders [4]. The most widely employed atomization types in the industries is vacuum induction gas atomization technology (VIGA) [5-6]. In recent years, a lot of research have been done on the VIGA technology, mainly focusing on the atomization flow field structure [7-10]. For example, Supersonic gas-flow and shock wave at the outlet of nozzle [11-12], Mechanism of primary and secondary atomization breakup [2,13], optimization design of nozzle [14] and Influence of different parameters on the gas-flow field structure of atomization chamber [15], it aims to improve the fine powder yield, and reduce the size distribution range.

However, in the actual industrial production, it is found that nozzle clogging is a serious problem in VIGA technology. since it could suffer from the cease of production, and the melted alloy will be wasted, which will seriously affect the production efficiency and increase the cost. Moreover, in the process of atomization, the coupling-length of the delivery-tube (CLDT) which does not match the nozzle will interfere with the trajectory of metal droplets in the recirculation zone, resulting in the occurrence of the nozzle clogging. Nozzle clogging is a complex and unpredictable process. Thus, the investigation on the formation mechanism of nozzle clogging at the tip of delivery-tube is critical for controlling the VIGA process. Recent years, many scholars have studied many aspects of the delivery-tube. Such as: Le & Henein [16] noted that in the atomization experiment of free-fall nozzle configuration, higher protrusion lengths of the delivery-tube will cause larger mass flow rate and lower GMR value; Srivastava & Ojha [17] reported that for change in delivery-tube in the range of a few millimeters, which will affect the particle size of the final powder; Zeoli et al. [18] Studied the influence of geometry and position of delivery-tube on atomization. The results show that the pressure at the tip of delivery-tube has a great

[1] UNIVERSITY OF SCIENCE & TECHNOLOGY BEIJING INSTITUTE OF SPECIAL CERAMICS AND POWDER METALLURGY, 30 XUEYUAN ROAD, HAIDIAN DISTRICT, BEIJING, 100083, CHINA
[2] UNIVERSITY OF SCIENCE & TECHNOLOGY ACADEMICIAN OF CAS, INSTITUTE OF SPECIAL CERAMICS AND POWDER METALLURGY, BEIJING, CHINA
* Corresponding author: xmdsg@ustb.edu.cn

relationship with the protrusion lengths. However, there are few systematic studies on the effect of CLDT on the nozzle clogging.

In this study, the nozzle clogging of gas atomization process at different CLDT is studied using numerical simulation and experimental methods. Volume of Fluid (VOF) model and the large eddy simulation (LES) model are employed to investigate the primary stage of the atomization for the nozzle. Hence, the present work attempts to understand the significance of the effect of alloy melt at the tip of the delivery-tube on the nozzle clogging. To obtain the formation mechanism of nozzle clogging, two inlet gas pressures (3 Mpa and 4.5 Mpa) are considered while keeping other parameters such as gas and melt physical properties, melt flow rates the same. Besides, the simulation results were verified by industrial test using Ni-based alloy as raw material. While solving the problem of nozzle clogging, the CLDT is controlled within a reasonable range through atomization experiments. This study provides a method to solve the problem of ladle nozzle clogging and optimize the properties, particle size and morphology of the powder that emerges potential of AM.

2. Experimental setup and methods

2.1. Experimental setup

The schematic of the setup used for atomizing molten Ni-based alloy is shown in Fig. 1. This atomization system consists of five main parts, namely cooling water circulation system, inert gas supply system (Argon), vacuum system, melting system, close-coupled nozzle system, and powder collection system. Melting was carried out in a magnesia crucible having a capacity of 100 kg and was heated by a high-frequency induction furnace. The Ni-based alloy melt temperature was measured using an infrared thermometer. Argon was conducted as the atomization gas for all the runs. Atomization pressures ranged from 1.0 to 5.0 MPa. Prior to the atomization test, when there is only gas flow, the capillary was inserted into the delivery-tube to measure, and the capillary was located at the tip of the delivery-tube, so it did not interfere with the gas turbulence intensity in the recirculation zone. The capillary was connected to the detector to obtain the aspiration pressure. The gas channel of close-coupled nozzle is convergent-divergent type for achieve atomization gas velocities that approach or exceed Mach 2.0. The angle of the flow channel at the gas outlet is 35°. The diameter of the atomization chamber is about 1.5 m and the height is 2.5 m, which is made of stainless steel. The delivery-tube is made of alumina ceramic with an inner diameter of 4 mm.

2.2. Experimental methods

In the industrial tests about 70 kg of Ni-based alloy were melted and over-heated to 1600°C. The tundish was heated by induction coils before the Ni-based alloy was started to maintain the temperature of the alloy melt during atomization. Before the alloy melt reached the delivery-tube, the atomizing gas was sent to the nozzle by opening the valve on the gas pipeline. The gas pressure was constant during atomization. After completing the experiment produced powders and used delivery-tube were collected. Then the residual powders on the surface of the atomizing chamber and the powder collecting tank were cleaned.

Fig. 2 shows the schematic of the annular nozzle used in this experiment. the design of convergent-divergent nozzle was first employed in Schwenck et al. [19]. Based on the range of

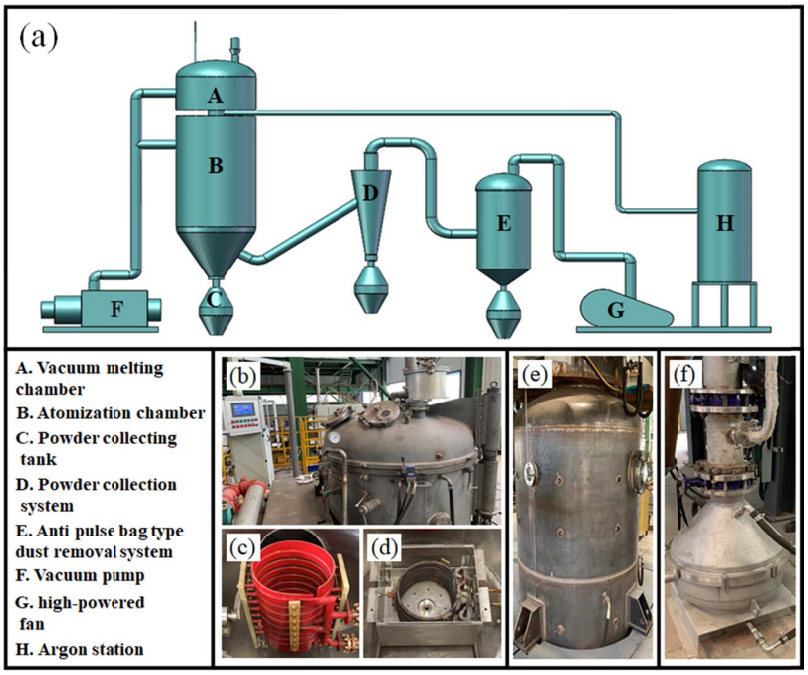

Fig. 1. (a) Schematic of the experimental setup, (b) Vacuum melting chamber, (c) High frequency induction power supply, (d) Close-coupled nozzle, (e) Atomization chamber, and (f) Powder collecting tank

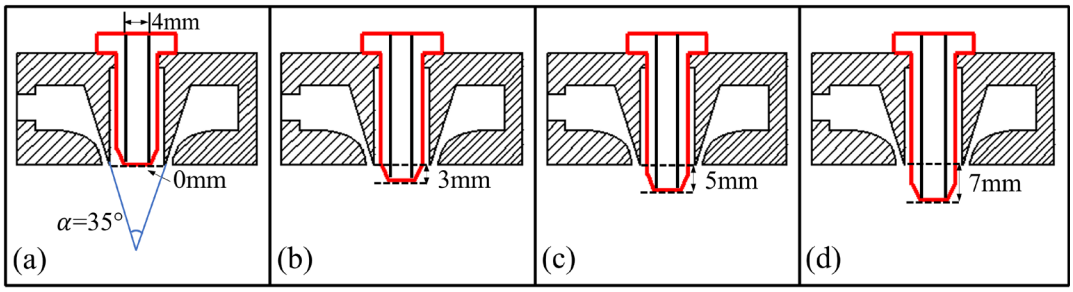

Fig. 2. Schematic depicting the CLDT with respect to the gas nozzle (a) 0 mm, (b) 3 mm, (c) 5 mm, and (d) 7 mm

TABLE 1

Composition and content of Ni-based alloy

Component	**Ni**	**Co**	**Cr**	**W**	**Ti**	**Al**
Content / %	45.70~46.20	20.00~22.00	12.00~14.00	4.10~4.50	3.30~3.70	3.30~3.70
Component	**Mo**	**Ta**	**Nb**	**C**	**B**	**Zr**
Content / %	2.50~2.90	1.40~1.80	1.30~1.70	0.02~0.04	0.02~0.03	0.04~0.07

TABLE 2

Experimental parameters in gas atomization of different CLDT

Ni-based alloy	**3MPa**				**4.5MPa**			
L_D (mm)	0	3	5	7	0	3	5	7
S_N (mm)	0.6	0.6	0.6	0.6	0.6	0.6	0.6	0.6
t_a (min)	—	18.5	14.7	12.1	—	16.3	13.2	10.8
T_G (K)	298	298	298	298	298	298	298	298
M_G (kg/h)	580	580	580	580	875	875	875	875
ΔT (K)	200	200	200	200	200	200	200	200
M_l (kg/h)	—	227.03	285.71	347.11	—	257.67	318.18	388.89
GMR	—	2.55	2.03	1.67	—	3.40	2.75	2.25

Note: L_D – coupling length of delivery-tube, S_N – slit width of gas-outlet, t_a – atomizing pouring time, T_G – atomization gas temperature, M_G – gas mass flow rate, ΔT – melt superheat, M_l – melt mass flow rate, GMR – gas-to-metal mass flow rate ratio.

the CLDT discussed in the previous literatures [15,17] and the actual industrial production, four different CLDT are selected, namely: 0 mm, 3 mm, 5 mm, and 7 mm, respectively. Atomization of the Ni-based alloy using argon gas was performed at two different gas pressures (3 MPa and 4.5 MPa). The composition of nickel base superalloy is shown in TABLE 1 and the general process parameters used are presented in TABLE 2. Particle size distribution of powders were analyzed using a Seishin LMS-30 laser particle sizer. The particle morphology was measured with LEO-150 SEM.

3. Numerical methods

3.1. Geometric model

According to the geometry of the nozzle used in the industrial test, the geometric model in the simulation was established using CAXA-CAD software and the multiphase-flow patterns have been calculated (Ni-based alloy and Argon). Furthermore, the resulting gas-flow fields were coupled to calculate Ni-based alloy melt to study the influence of the flow field on the melt flow and to gain a better understanding of the mechanisms leading to nozzle clogging. The geometric model included three portions, i.e., the gas passage within the nozzle, delivery-tube and atomization chamber field. The structure and size of the model were determined by measuring the nozzle used in the industrial experiment. In general, the geometric models of nozzle (70 mm×150 mm) are simplified compared to the physical device, in order to reduce the amount of simulation time. The geometric model of nozzle used in simulation calculation is depicted in Fig. 3(a).

3.2. Boundary conditions

The solver of simulation calculation used is the CFD 19.0. The conditions for the pressure of the atomization chamber outlet were set to the standard atmospheric pressure, i.e., 101,325 Pa. The atomizing gas used is argon. The inlet boundary of the nozzle was set as the pressure-inlet conditions. For the Ni-based alloy tracking calculations, the melt velocity was 2 m/s. The velocity-inlet conditions at the delivery tube were based on the given mass flow rate of melt derived from the experiments. In

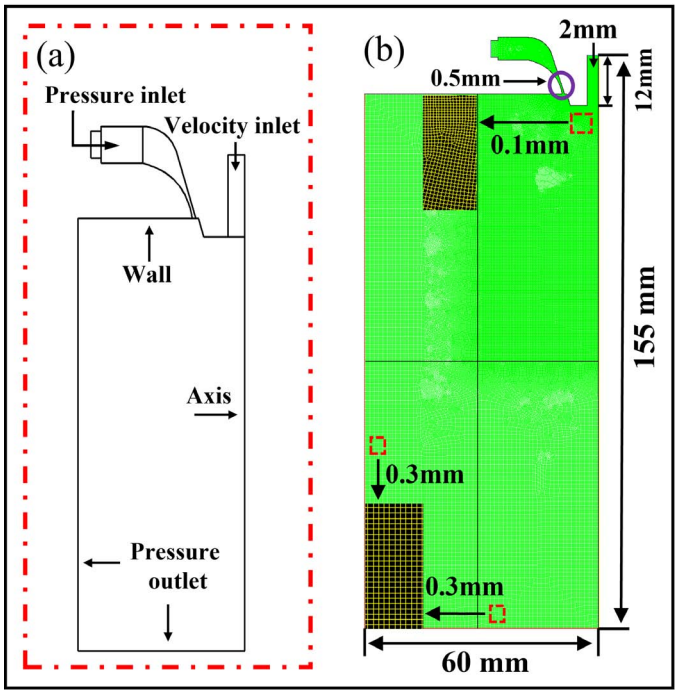

Fig. 3. (a) boundary conditions and computational domain, (b) used mesh for the CFD model

the center of the model, an axial symmetry condition was used as shown in Fig. 3(a). The residual geometric model boundary was set as the wall type. The non-slip boundary was employed to the surface of the inner wall. The surface tension coefficient between argon and alloy was set to 1.84 N/m. The calculated physical parameters of both materials (Argon and Alloy) settings are listed in TABLE 3 and 4. The specific simulation boundary conditions are shown in TABLE 5.

3.3. Meshing setting

Fig. 3(b) depicts the schematic of meshing setting for primary atomization simulation. The atomization field of the close-coupled nozzle was meshed using the preprocessing software GAMBIT. The mesh size was set by applying the size function. The interval size of the high-pressure gradient zone near the nozzle and the wall was set to 0.1 mm, and the interval size of the pressure outlet zone of the atomization chamber was set to 0.3 mm. the initial grid number of cells was 124601. In the primary atomization area at the tip of the delivery tube, for capture finer alloy melt droplets, the adaptive mesh refinement method was used to encrypt the grid. The final grid has a cell number of 512739, which indicates that extensive refinement is obtained in the positions of primary atomization recirculation zone. Markus et al. [20] reported that the droplet size after the primary atomization breakup is about 10%-100% of delivery-tube diameter. Since the diameter of the delivery-tube is 4 mm, the dynamic mesh refinement is sufficient to meet the accuracy requirements of simulation in the primary atomization process.

TABLE 3

Physical parameters of Argon

Properties	Value
Heat capacity ($J \cdot kg^{-1} \cdot K^{-1}$)	520.65
Thermal conductivity ($W \cdot m^{-1} \cdot K^{-1}$)	0.016
Molecular weight (kg·mol−1)	39.95
Viscosity ($kg \cdot m^{-1} \cdot s^{-1}$)	2.125×10^{-5}

TABLE 4

Physical parameters of Ni-based alloy

Properties	Value
Density ($kg \cdot m^{-3}$)	7055.84
Viscosity ($kg \cdot m^{-1} \cdot s^{-1}$)	0.05
Thermal conductivity ($W \cdot m^{-1} \cdot K^{-1}$)	29.6
Molecular weight ($kg \cdot mol^{-1}$)	48
Heat capacity ($J \cdot kg^{-1} \cdot K^{-1}$)	720

TABLE 5

Initial boundary conditions for simulation

Boundary conditions	Value
Pressure inlet (MPa)	3.0/4.5
Pressure outlet (MPa)	0
Velocity inlet ($m \cdot s^{-1}$)	2
Temperature (k) (Argon/Alloy)	300/2000
Volume fraction (Argon/Alloy)	0/1

3.4. atomization breakup model

The mass conservation, energy conservation and momentum conservation of fluid flow field are obtained from the Navier-Stokes (N-S) equations, and the fluid variables in the calculation process are decomposed into mean value and fluctuation value [21]. The decomposition velocity is as follows:

$$u(t) = u + u'(t) \tag{1}$$

In order not to directly simulate small-scale turbulent flow, N-S equations is transformed into Reynolds Averaging Navier-Stokes (RANS) equations. The RANS equations are the control equation of flow field average variable. The RANS continuity equation of compressible flow is as follows [21]:

$$\frac{\partial \rho}{\partial t} + \frac{\partial}{\partial x_i}(\rho u_i) = 0 \tag{2}$$

the RANS momentum equation:

$$\frac{\partial}{\partial t}(\rho u_i) + \frac{\partial}{\partial x_j}(\rho u_j u_i) = -\frac{\partial p}{\partial x_i} + \frac{\partial \sigma_{ij}}{\partial x_j} + \frac{\partial}{\partial x_j}\left(-\rho \overline{u_i' u_j'}\right) \tag{3}$$

Where u_i is the Reynolds average velocity component with the average sign omitted, ρ is the density, P is the pressure, u_i' is the pulsating velocity, and σ_{ij} is the stress tensor component.

The VOF multiphase flow model with interface tracking capability was performed to simulate the atomization process for the limited nozzle. Using the VOF model we could simulate the flow between the multiphase superalloy and argon, by solving a separate momentum-equation and dealing with the volume fraction for each phase of the fluid that passes through the region [22]. The used mathematical expression is:

$$\frac{\partial \alpha_q}{\partial t} + v_q \cdot \nabla \alpha_q = \frac{S_{\alpha_q}}{\rho_q} + \frac{1}{\rho_q} \sum_{p=1}^{n} \left(\dot{m}_{pq} - \dot{m}_{qp} \right) \tag{4}$$

Here, $\dot{m}_{pq}$ is the mass transfer from the P phase to the q phase, and $\dot{m}_{qp}$ is the mass transfer from the q phase to the P phase. Generally, by default, the source phase on the right side of the formula is zero.

In the VOF multiphase flow model, the momentum equation is solved by solving a single momentum equation in the whole region. As a result, the velocity field is shared by each term. The momentum equation depends on the volume fraction of all phases for the attributes ρ and μ [22]. Hence:

$$\frac{\partial}{\partial t}\left(\rho \vec{v}\right) + \nabla \cdot \left(\rho \vec{v} \vec{v}\right) = \\ = -\nabla P + \nabla \cdot \left[\mu \left(\nabla \vec{v} + \nabla \vec{v}^T \right) \right] + \rho \vec{g} + \vec{F} \tag{5}$$

Using the VOF multiphase flow-model, the energy equation is also shared, which can be expressed as follows:

$$\frac{\partial}{\partial t}\left(\rho E\right) + \nabla \cdot \left[\vec{v} \left(\rho E + p \right) \right] = \nabla \cdot \left(k_{eff} \nabla T \right) + S_h \tag{6}$$

The VOF multiphase flow model deals with the energy equation phase E and the temperature T as the average mass:

$$E = \frac{\sum_{q=1}^{n} \alpha_q \rho_q E_q}{\sum_{q=1}^{n} \alpha_q \rho_q} \tag{7}$$

The LES model was adopted to visualize the fine droplets of atomized metal flow. Compared with other models, the LES model can filter out turbulence and divide it into large and small eddies. Menon et al. [23] proposed a sub-grid kinetic energy model. The transport equation for this model is as follows:

$$\frac{\partial \left(\bar{\rho} \overline{k^{sgs}} \right)}{\partial t} + \frac{\partial \left(\overline{\rho u_j} \overline{k^{sgs}} \right)}{\partial x_j} = \\ = -\tau_{ij}^{sgs} \frac{\partial \overline{u_j}}{\partial x_j} + \varepsilon^{sgs} - \frac{\partial}{\partial x_j} \left(\frac{v_t \partial k^{sgs}}{\sigma_k \partial x_j} \right) \tag{8}$$

where k^{sgs} is the sub-grid kinetic energy, τ^{sgs} is the sub-grid stress, v_t is the sub-grid viscosity coefficient, ε^{sgs} is the turbulent energy dissipation rate, and u_j is the velocity.

4. Results and discussion

4.1. Introduction of the nozzle clogging in industrial production

For further intuitively understand the phenomenon of the nozzle clogging in the atomization process, a camera was employed to capture the movement of the droplets. Fig. 4 displays the images of the atomization state of the alloy melt at different times when the CLDT is irrational. The atomization of alloy liquid flow at the tip of the delivery-tube is instable as can clearly be seen in the images. For the 1364 ms, as shown in Fig. 4(b), the area of recirculation zone becomes smaller, the fine powder nephogram obtained by secondary atomization disappears, and the atomization morphology changes from cone to cylinder. At t = 1691 ms shown in Fig. 4(c), the alloy liquid column hanging at the bottom of the delivery-tube breaks due to its gravity action. However, the residual alloy melt adhering to the edge of the delivery-tube solidifies after encountering low temperature gas, and the nozzle is blocked. In an attempt to explain this phenomenon observed in the atomization process, CFD simulation has been carried out to provide further understanding of the nozzle clogging behavior around the tip of the melt delivery-tube external wall.

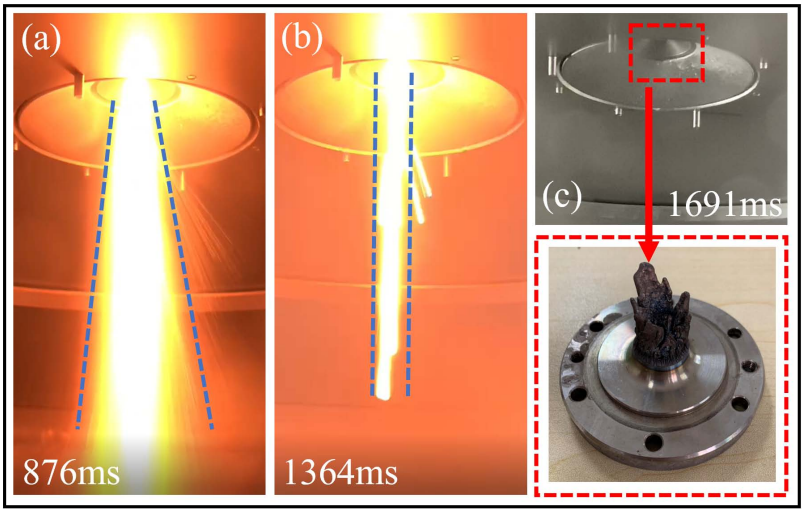

Fig. 4. Images of the alloy melt movement captured by a camera during atomization process

4.2. Mechanism analysis of the nozzle clogging behavior

Fig. 5 shows the nozzle clogging process of primary atomization at the tip of the delivery-tube in the VIGA industrial test. It can be clearly seen that the primary atomization is carried out in the recirculation zone at 0.33 ms. The edge of umbrella shaped structure [24] becomes thinner under the action of the pulsating shearing force and the surface wave. After reaching the critical value, the liquid ligament breaks up and moves with the flow direction.

For clarity, the breakup state of the alloy melt is marked with purple and yellow circles, respectively. The purple labeled ligaments separated from the alloy melt around 0.43 ms. During the upward movement, from 0.33 ms to 0.53 ms, this indicates that the alloy melt undergoes Rayleigh-Plateau instability [25] and the gas generates more perturbations on the surface of melt. The ligaments then collapsed under the action of gas intensity due to surface tension and many irregular spheres (droplets) were formed, and finally cohered to the surface of the delivery-tube. However, under the driving force of the gas-flow in the recirculation zone, the ligaments marked in yellow continued to extend upward due to instability. It can be observed that the reflux melt ligament solidifies at the tip of the delivery-tube in a very cold expanding gas environment. Over a short period, a layer of alloy melt was attached to the tip of the delivery-tube,

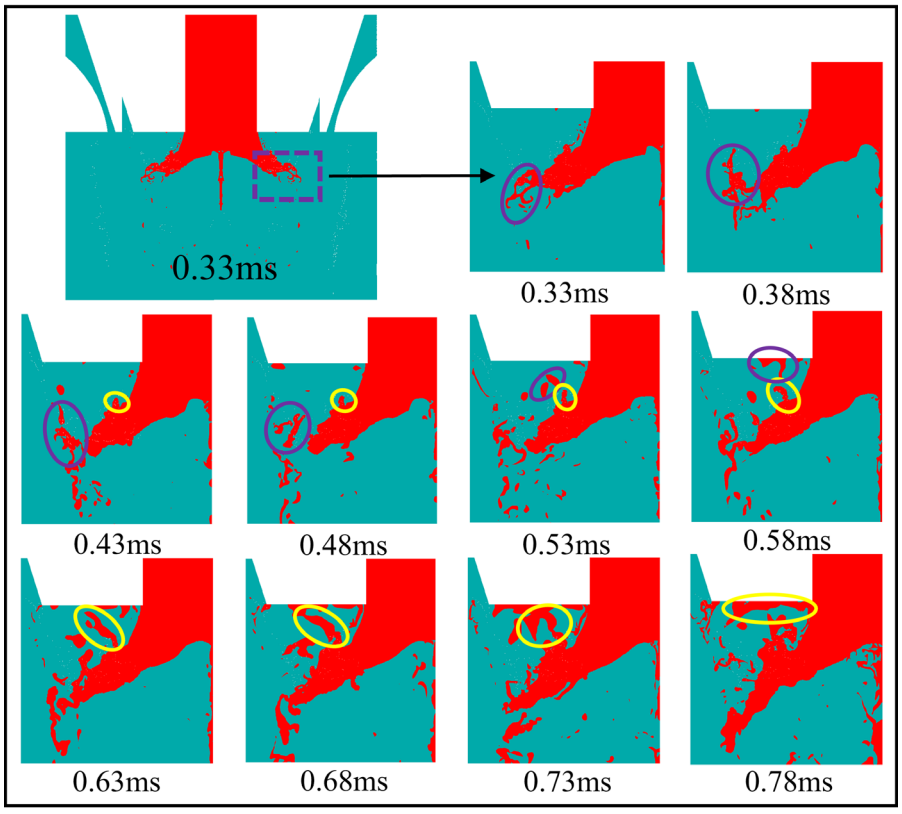

Fig. 5. Formation mechanism of nozzle clogging during alloy melt atomization

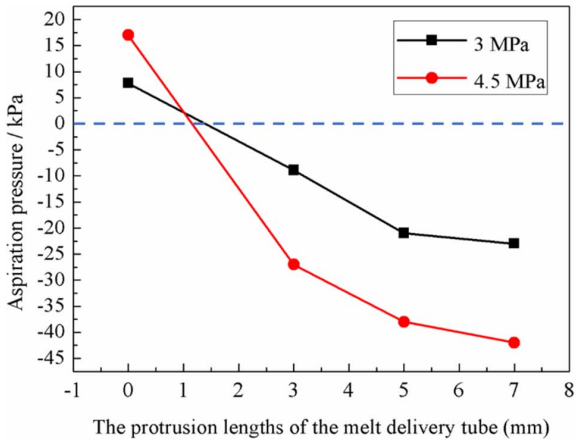

Fig. 6. Gas aspiration pressure at the tip of the melt delivery tube for different CLDT for gas only flow

which repeated periodically until the nozzle clogging occurred and the atomization stopped. As a result of this it is important to determine the optimum design for the external melt CLDT. The mechanism of its influence on the gas-flow field and the primary atomization will be discussed below.

4.3. Influence of different CLDT on nozzle clogging

4.3.1. Aspiration pressure

Aspiration pressure measurements are carried out at the tip of the four different CLDT. Fig. 6 shows the aspiration pressure as a function of the CLDT included under different atomization gas pressure conditions (3.0 MPa and 4.5 MPa). It can be seen

in Fig. 6 that the aspiration pressure changes with CLDT. The tip of the delivery-tube was always under positive pressure value in the atomization gas pressure range of 3.0-4.5 MPa for the coupling-length of 0 mm. Resulting in the positive pressure in the recirculation zone resists the free fall of the molten metal at the tip of the delivery-tube. This will, however, inevitably lead to "freezing up" at the nozzle [16]. However, compared with 0 mm, there is always negative pressure at the tip of the melt delivery-tube for 3, 5 and 7 mm coupling-lengths, which is conducive to the free fall of the alloy melt, whereas the excessive aspiration pressure will increase the mass flow rate of the melt under the same atomization pressure and resulting in the final particle diameter becoming coarser. The data obtained from measurement depicts that the longer is the coupling-length, the higher is the negative pressure value at the tip.

4.3.2. Gas-flow field

In the gas-flow field (no alloy melt), the gas jet converges at a certain angle under the restriction of close-coupled nozzles. At the same time, after supersonic flow meets stagnation point, a part of the airstream reverses and flows upward along the axial direction, forming a recirculation zone below the delivery-tube. Fig. 7(a) and 7(b) show the comparison clouds of the gas-flow field for the atomization pressure of 3 MPa and 4.5 MPa, respectively. For the 0 mm, as shown in Fig. 7(a), the position of recirculation zone is the highest and the closest to the tip of the delivery-tube. The upward gas velocity in Fig. 8(a) is found to be approximately 200 m/s, which hinders the flow of alloy melt in the delivery-tube to a certain extent, and even makes it reverse flow, resulting in the alloy flow solidified on

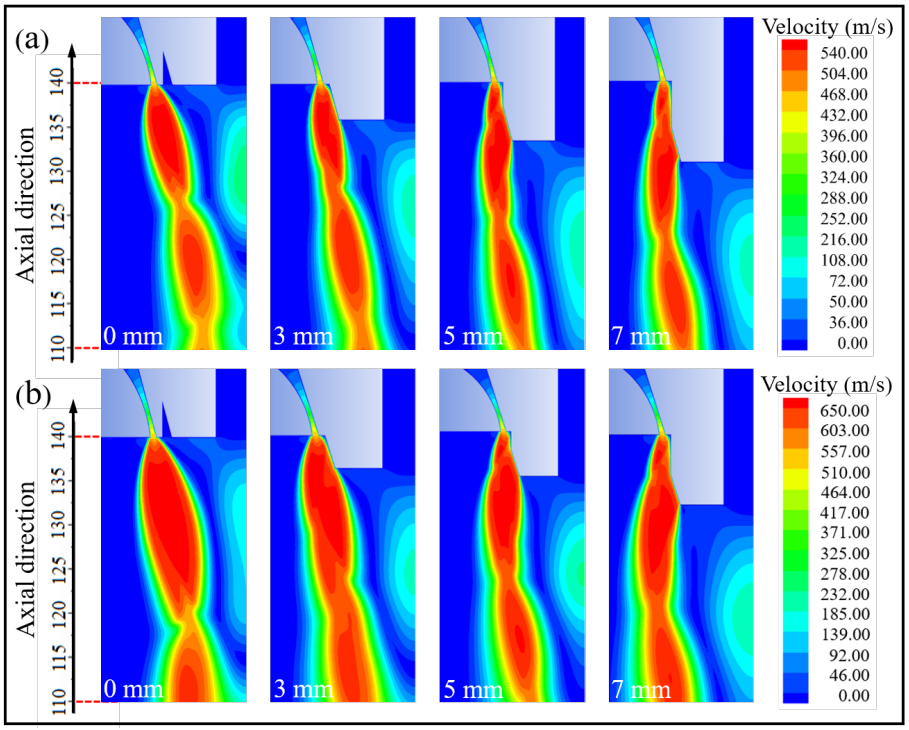

Fig. 7. Velocity nephogram of the different CLDT: (a) 3 MPa, (b) 4.5 MPa

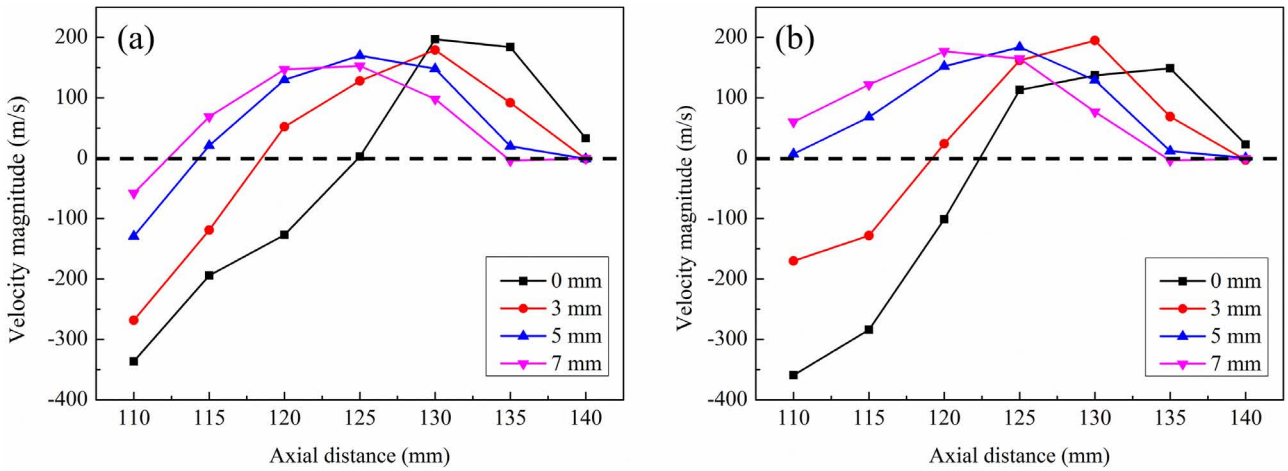

Fig. 8. Comparison of axial velocity with different CLDT: (a) 3 MPa, (b) 4.5 MPa

the surface of the delivery-tube and blocked the nozzle in the low temperature atomization gas environment. However, with the extension of the CLDT, it can be observed that the position of the recirculation zone moves downward, and the velocity of the gas-flow is about 90 m/s at 7 mm, which promotes the flow of alloy molten and largely avoids the occurrence of nozzle clogging.

It can be found from the cloud diagram of the gas-flow field that there are a series of shock waves at the nozzle exit. When the gas is completely expanded, a negative pressure gradient near the free boundary acoustic velocity. The region of sub-ambient pressure causes the alloy flow to be sucked onto the surface of the delivery-tube from the primary atomization crushing position. When the coupling-length of the delivery-tube is 0 mm, as shown in Fig. 7(a), the atomized gas is compressed through the Laval channel and expands at the gas outlet. Because there is no obstruction near the outer wall of the delivery-tube close to the gas outlet, the compressed atomized gas can expand completely. However, in increasing the CLDT to 5 mm, the gas shows under-expanded behavior, and further expansion will occur far away from the exit, resulting in no negative pressure area between the outer wall of the delivery tube and the sonic boundary. This demonstrates that the chance of nozzle clogging with 5 mm or 7 mm coupling-lengths is significantly reduced. The same trend can also be seen in fig. 7(b) when the pressure value is 4.5 MPa. The axial velocity of 0 mm shown in Fig. 8(b) is less than that of other coupling-lengths. This is due to the appearance of double recirculation zone, which reduces the gas-flow intensity [18], this section does not explain too much.

4.3.3. Comparison of atomization simulation and experimental results

Fig. 9(a) shows the comparison of numerical simulation and experimental results of the CLDT respectively under the atomization pressure of 3Mpa. This indicates that with the increase of the CLDT, the alloy melt cohered on the tip of the draft tube decreases gradually. For 0 mm, as shown in Fig. 9(a_1), large amounts of ligaments and droplets move under the delivery-tube and randomly adhere to the surface at the atomization process. As there is no obstruction of the outer wall of the delivery-tube, the atomizing gas expands rapidly after leaving the nozzle, the free boundary of the supersonic gas shrinks along the radial direction, and the area of the recirculation zone decreases, resulting in the shape of the alloy melt in the final nozzle clogging is conical. For 3 mm, droplets and liquid lines of alloy melt below the delivery-tube in Fig. 9(a_2) are found to decrease, and the protruding outer wall of the delivery-tube restricts the free boundary of the gas to move inward. However, with the layer by layer bonding of alloy melt at the tip of the delivery-tube, the nozzle clogging will not appear as quickly as 0 mm, but will be in a semi blocked state, which will reduce the melt diameter during atomization, and the reduced mass flow rate will increase the GMR value, resulting in a wider particle size distribution of the final powder, which is not conducive to industrial production demand. It can be seen from Fig. 9(a_3) and Fig. 9(a_4) that there is no alloy melt accumulated on the outer wall of the delivery-tube, which is consistent with the photos of the delivery-tube after the test under the same conditions, and the atomization

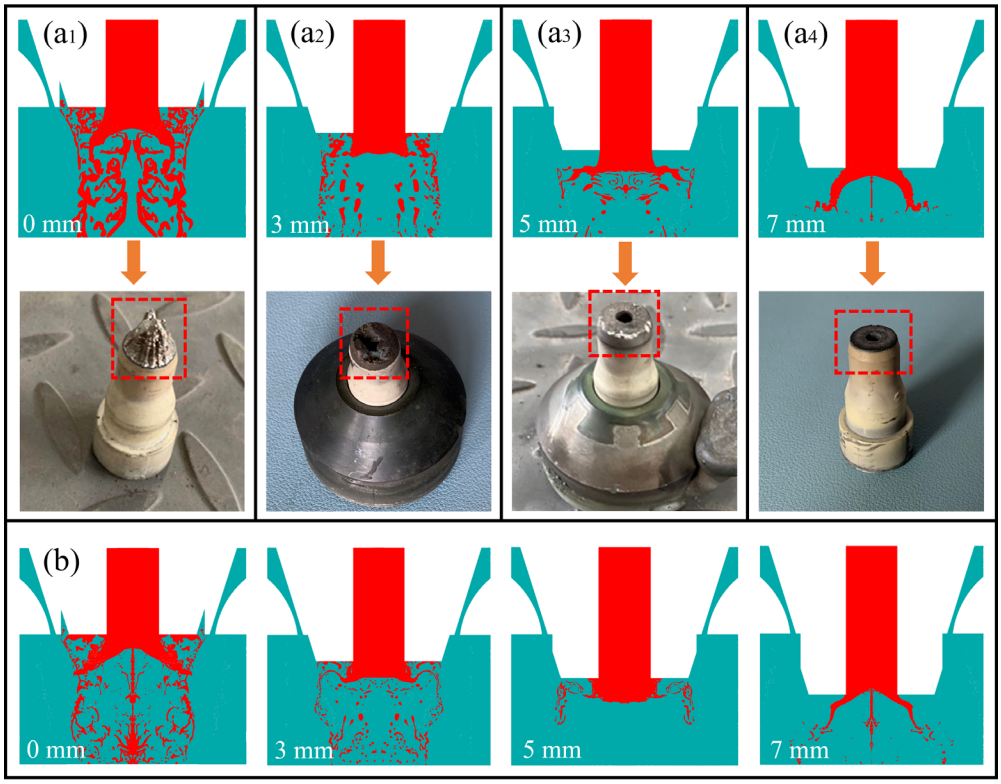

Fig. 9. Comparison between numerical simulation and experimental results: (a) atomization pressure of 3 Mpa, (b) atomization pressure of 4.5 Mpa

process is continuous. This demonstrates that the lower strength (momentum) of the recirculation zone for the coupling-length of 5-7 mm, and the coupling distance of the delivery-tube prevents the full expansion of the high-pressure gas, thus losing the jet momentum and reducing the turbulent kinetic energy of the flow in the recirculation zone. The same trend can be seen in the simulation results when the atomization pressure is 4.5 MPa. As shown in Fig. 9(b), the increasing of atomization pressure increases the position of recirculation zone, which is conducive to the improvement of fine powder yield, but also increases the probability of nozzle clogging.

TABLE 5 shows the number of atomizing furnaces and atomizing time in continuous service of delivery-tube under the condition of different CLDT. It can be found from TABLE 5 that the number of times the delivery-tube is used increases with the increase of the CLDT. The CLDT of 0 mm causes nozzle clogging at the beginning of atomization. When the coupling length is 3 mm, the number of atomization heats is only two, and the atomization time of the second heat is greatly increased because the delivery-tube is semi blocked after the end of the first heat. However, when the CLDT is 5 mm and 7 mm, the use times increase significantly, reaching 5 and 6 times, respectively. Finally, due to the residual alloy melt and internal cracking at the inlet of the delivery-tube, the recycling is stopped. From Fig. 10, it can be observed that the total atomization time of the 5 mm and the 7 mm are not far apart (96 minutes and 91.5 minutes respectively). During this process, there is no nozzle clogging, and the atomization process is continuous and stable.

Taking the coupling-length of 5 mm as an example, a camera is used to capture the atomization process of alloy melt at 3 Mpa. Fig. 11 displays the images of the alloy melt flowing out of the delivery-tube and moving to the atomization chamber under the condition of 5 mm. With the increase of the atomization time, the atomization recirculation zone becomes larger and moves downward. At 3s, the strength of recirculation zone is unstable and the atomization efficiency is reduced. After 12s, the recirculation zone areas on the picture basically remained unchanged. The atomization of the descending molten steel is smooth, moreover, no blockage of the delivery-tube was found.

TABLE 5

Statistics of atomization time of each furnace under the different CLDT. (min)

CLDT/mm	Number of heats					
	1st	2nd	3rd	4th	5th	6th
0	—	—	—	—	—	—
3	18.5	26.2	—	—	—	—
5	14.7	16.1	18.5	21.4	25.3	—
7	12.1	12.6	13.2	15.5	17.2	20.9

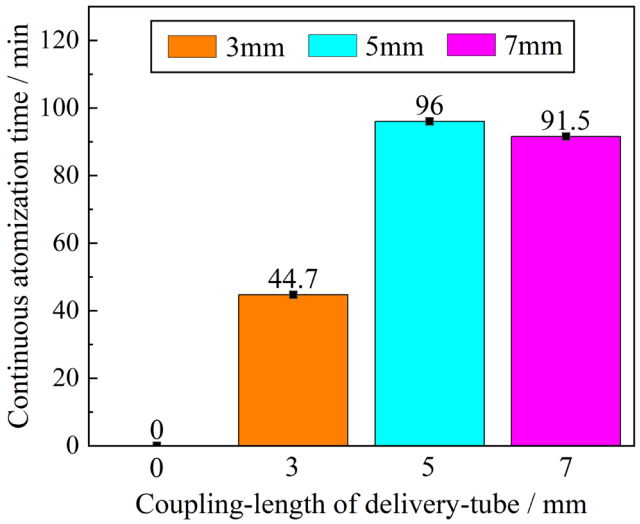

Fig. 10. The total atomization time of each delivery-tube for the CLDT

The rule obtained by the experiment is the same as the simulation, which further proves the correctness of the simulation.

4.3.4. Powder morphology

Comparative simulation and experimental results are found that the atomization trend of 4.5 MPa is close to that of 3 MPa. Therefore, this section only enumerates the SEM images of different CLDT (3 mm, 5 mm, and 7 mm) powders prepared under

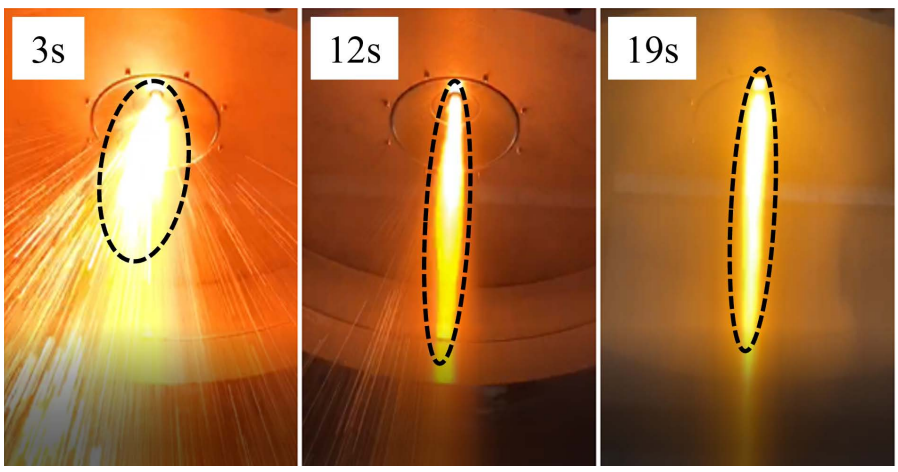

Fig. 11. Images of the alloy melt injection captured by a camera during atomization process under the 5 mm

the atomization pressure of 3 MPa as shown in Fig. 12 (Due to the coupling-length of 0 mm, the nozzle is completely blocked, so it is not considered). The micrographs of the Ni-based alloy powder samples, as presented in Fig. 12(a), indicate that the particles generated with a coupling-length of 3 mm are more spherical and smoother, and the particle size is smaller than that of the delivery-tube with the coupling-length of 5 mm (Fig. 12(b)). This is due to the accumulation of a lot of backflow alloy droplets at the tip edge of the delivery-tube during the primary atomization process, resulting in the actual diameter of the melt column smaller than the inner diameter of the delivery-tube, thus reducing the mass flow rate and leading to the formation of fine powder. Moreover, it is clearly visible that the powders generated with a coupling-length of 7 mm exhibit a lot of satellites sticking on the surface of larger particles compared with those generated with the coupling-lengths of 3 mm and 5 mm. The red dotted line marks represent insufficiently broken and short rod-shaped particles, as shown in Fig. 12(c), which demonstrates that when the coupling-length is 7 mm, the higher aspiration pressure in the recirculation zone leads to the increase of the mass flow rate of the alloy melt, resulting in the fine particles adhering to the surface of the large droplet which is not completely solidified, forming a large number of satellite powders, further reducing the powder fluidity and apparent density. This indicates that the CLDT should be controlled in a suitable range to improve the yield of fine powder after the condition of solving the nozzle clogging. Due to the limited number of particles described, SEM images cannot give a completely representative overview, so the measurement results in Fig. 13 must be considered.

4.3.5. Particle size distribution

When the CLDT is 0mm, the phenomenon of the nozzle logging will occur shortly after the atomization experiment is started. Therefore, Only the particle size distribution of powders prepared of 3 mm, 5 mm and 7 mm is detected at a gas pressure of 3 MPa, as shown in Fig. 13 comparing the three kinds of powders indicates that the median diameter has increased with an increase in the CLDT. Increasing the CLDT leads to an reduction of gas momentum in recirculation zone and therefore the kinetic energy that is not enough to disintegrate the alloy melt. Laser particle size determination shows the resultant CLDT of 3 mm has a wide particle size distribution with median particle size less than 35 μm. The reason is that the inner diameter of the delivery-tube becomes smaller due to the alloy melt sticking on

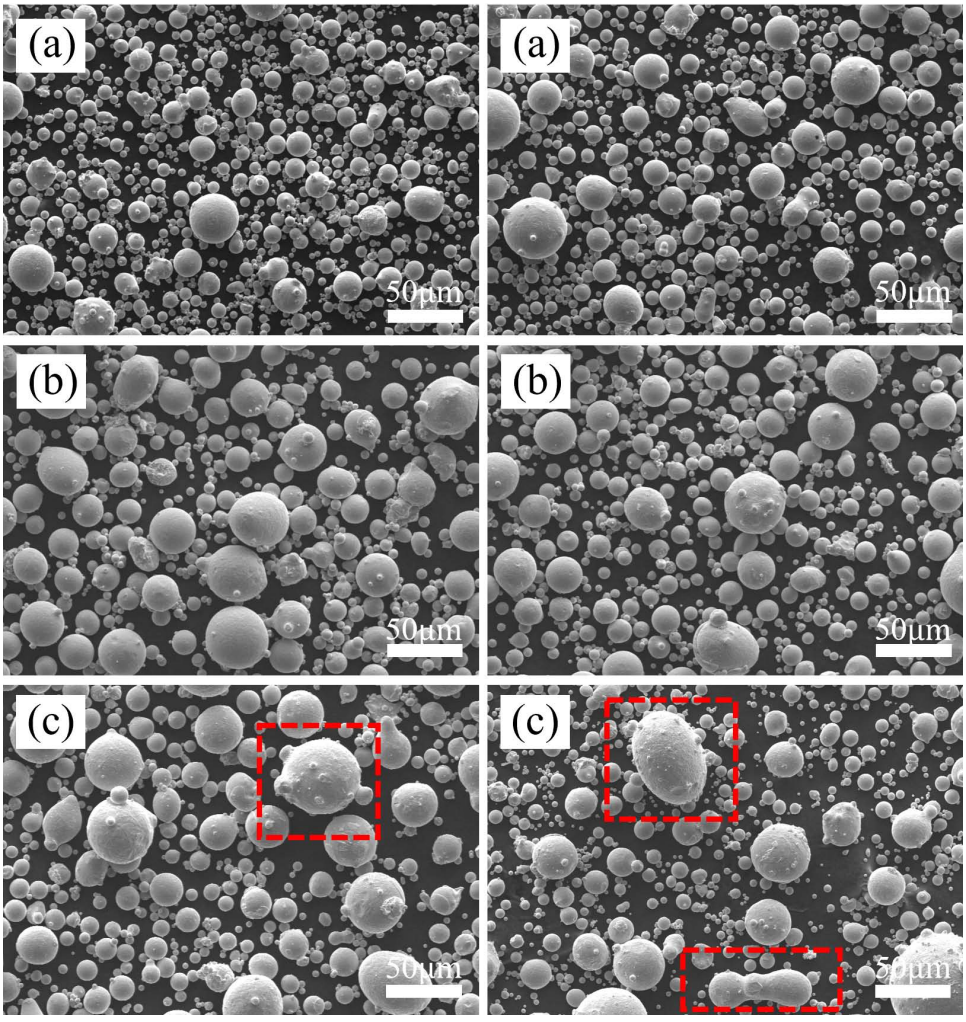

Fig. 12. SEM images of alloy powder with different CLDT: (a) 3 mm, (b) 5 mm, and (c) 7 mm

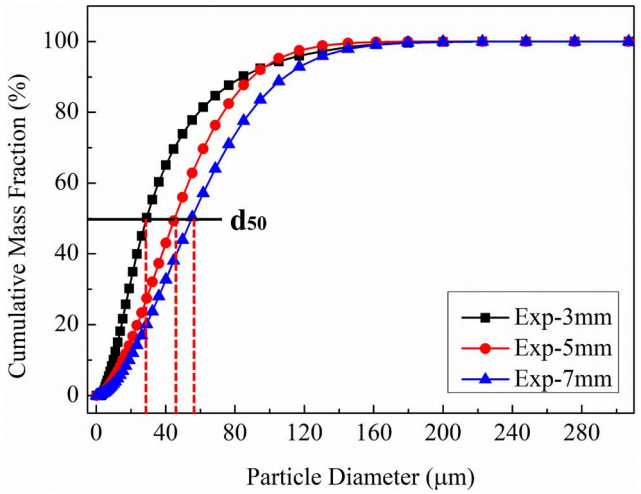

Fig. 13. Variation of cumulative mass percentage of Ni-based alloy powders with particle diameter for a gas pressure of 3 MPa

the tip of the delivery-tube during the atomization process, so that the finer alloy liquid column is easier to be broken. Additionally, it is clear that, for 7 mm conditions, the particle sizes are shifted to larger values due to the higher GMR [26] in general.

5. Conclusion

In order to solve the problem of frequent nozzle clogging in close-coupled atomization process, a new changing CLDT design scheme was developed. Therefore, CFD numerical simulations were conducted for different CLDT to estimate the influence of the coupling-length on the nozzle clogging. The achieved results showed that, with the suitable coupling-length, the nozzle clogging could be avoided, and a more stable atomization process can be obtained.

(1) The VOF model and LES model were employed to effectively predict the movement trajectory of alloy particles at the tip of the delivery-tube and explain the formation mechanism of nozzle clogging when CLDT mismatches in the primary atomization process. The predicted results were consistent with the industrial test, and the simulation method and mathematical model are verified.

(2) With an increase in the CLDT, the average particle size of the powder increased. When the CLDT was different, the morphology of the powder also varied significantly. At a larger coupling-length (7 mm), due to the smaller GMR and insufficient breakup, more irregular powder was formed (ellipsoid shape and short-rod shape). An excessive coupling-length also resulted in a large amount of satellite particles.

(3) In conclusion, these initial experiments show that using nozzle with CLDT ≥ 5 mm leads to a continuous atomization process without the risk of the nozzle clogging. In terms of powder properties, 5 mm shows either the better performance (particle circularity and narrow size distribution) compared to the 3 mm and 7 mm.

Data Availability Statements

The datasets generated and analysed during the current study are available from the corresponding author on reasonable request.

Declaration of interests

The authors declare that they have no known competing financial interests or personal relationships that could have appeared to influence the work reported in this paper.

Acknowledgments

This research work was supported by Central University Basic Research Fund of China, FRF-GF-19-0058.

REFERENCES

[1] S. Motaman, A.M. Mullis, R.F. Cochrane, D.J. Borman, Numerical and experiment investigations of the effect of melt delivery nozzle design on the open-to closed-wake transition in closed-coupled gas atomization, Metall. Mater. Trans. B. **46**, 1990-2004 (2015).

[2] D. Singh, S. Dangwal, Effects of process parameters on surface morphology of metal powders produced by free fall gas atomization, J. Mater. Sci. **41** (12), 3853-3860 (2006).

[3] R. Metz, C. Machado, M. Houabes, J. Pansiot, M. Elkhatib, R. Puyane, M. Hassanzadeh, Nitrogen spray atomization of molten tin metal: Powder morphology characteristics, J. Mater Process. Tech. **195** (3), 248-254 (2007).

[4] N. Zeoli, S. Gu, Computational simulation of metal droplet breakup, cooling and solidification during gas atomization, Comput. Mater. Sci. **43** (2), 268-278 (2008).

[5] J. Ting, I.E. Anderson, A computational fluid dynamics (CFD) investigation of the wake closure phenomenon, Mat. Sci. Eng. A. **379** (1), 264-276 (2004).

[6] S.P. Mates, G.S. Settles, A study of liquid metal atomization using close-coupled nozzles, part 2: atomization behavior, Atomization Spray **15** (1), (2005).

[7] O. Aydin, R. Unal, Experimental and numerical modeling of the gas atomization nozzle for gas flow behavior, Comput. Fluids **42** (1), 37-43 (2011).

[8] S. Feng, M. Xia, C.C. Ge, An EIGA driven coupled of electromagnetic-thermal field modeling in the induction melting process, Int. J. Mater. Form. **12** (4), 615-622 (2019).

[9] R.P. Guo, L. Xu, Y.P. Zhong, R. Yang, Characterization of Prealloyed Ti-6Al-4V Powders from EIGA and PREP Process and Mechanical Properties of HIP Powder Compacts, Acta. Metall. Sin-Engl. **30** (8), 735-744 (2017).

[10] M. Xia, P. Wang, X.H. Zhang, C.C. Ge, Computational fluid dynamic investigation of the and secondary atomization of the free-fall atomizer in electrode induction melting gas atomization process, Acta. Phys. Sin-Ch. Ed. **67** (2018).

[11] N. Hansen, X. Huang, Structural Refinement of Interstitial Free (IF) Steel by Deformation and Phase Transformation, Mater. Sci. Forum **475** (3), 7-42 (2005).

[12] Y. Bai, T. He, D. Guo, X.T. Liu, F.Y. Shao, Y.D. Liu, Texture Evolution, Formability and Ridging Resistance of a Sn-bearing Ferritic Stainless Steel Under Different Hot Band Annealing Temperatures, Acta. Metall. Sin-Engl. **32** (11), 1362-1372 (2019).

[13] A. Montadhar, J.S. Alan, F. Masoumeh, C. Stephen, Estimation of the Temperature in the Stirred Zone and Cooling Rate of Friction Stir Welding of EH46 Steel from TiN Precipitates, Metall. Mater. Trans. A. **50** (11), 5103-5116 (2019).

[14] S.P. Mates, G.S. Settles, A study of liquid metal atomization using close-coupled nozzles, Part 1: Gas dynamic behavior, Atomization Spray **15** (1) (2005).

[15] I.E. Anderson, R.L. Terpstra, Progress toward gas atomization processing with increased uniformity and control, Mat. Sci. Eng. A. **326** (1), 101-109 (2002).

[16] T. Le, H. Henein, Effect of nozzle geometry and position on gas atomization, Int. J. Powder Metal. **32**, 353-364 (1996).

[17] V. Srivastava, S. Ojha, Effect of aspiration and gas-melt configuration in close coupled nozzle on powder productivity, Powder Metall. **49** 213-218 (2006).

[18] N. Zeoli, S. Gu, Computational validation of an isentropic plug nozzle design for gas atomization, Compute. Mater. Sci. **42** (2), 245-258 (2008).

[19] D. Schwenck, N. Ellendt, L. Mädler, Generation of small batch high quality metal powder, Powder Metall. **57**, 171-175 (2014).

[20] S. Markus, U. Fritsching, K.M. Bauckhage, Mater. Sci. Engin. A. **326**, 122 (2002).

[21] J. Ting, M.W. Peretti, W.B. Eisen, The effect of wake-closure phenomenon on gas atomization performance, Mat. Sci. Eng. A. **326** (1), 110-121 (2002).

[22] X.Q. Song, Y.X. Li, M. Han, Effect of liquid guide tube pressure on atomization efficiency and powder properties of Ni-based alloy, Powder Metall. **28** (1), (2018).

[23] S. Menon, P.K. Yeung, W.W. Kim, Effect of subgrid models on the computed interscale energy transfer in isotropic turbulence, Comput. Fluids **25**, 165-180 (1996).

[24] S. Spitans, H. Franz, E. Baake, Numerical Modeling and Optimization of Electrode Induction Melting for Inert Gas Atomization (EIGA), Metall. Mater. Trans. B. **51** (5), 1918-1927 (2020).

[25] Anderson, R. Figliola, H. Morton, Flow mechanisms in high pressure gas atomization, Mater. Sci. Eng. A. **148**, 101-114 (1991).

[26] H. Lubanska, Correlation of spray ring data for gas atomization of liquid metals, J. Met. **22**, 45-49 (1970).